Controlled partial interpenetration in metal–organic frameworks

Alan Ferguson[1], Lujia Liu[1], Stefanus J. Tapperwijn[1], David Perl[1], François-Xavier Coudert[2], Stijn Van Cleuvenbergen[3], Thierry Verbiest[3], Monique A. van der Veen[4] and Shane G. Telfer[1]*

Interpenetration, the entwining of multiple lattices, is a common phenomenon in metal–organic frameworks (MOFs). Typically, in interpenetrated MOFs the sub-lattices are fully occupied. Here we report a family of MOFs in which one sub-lattice is fully occupied and the occupancy level of the other can be controlled during synthesis to produce frameworks with variable levels of partial interpenetration. We also report an 'autocatenation' process, a transformation of non-interpenetrated lattices into doubly interpenetrated frameworks via progressively higher degrees of interpenetration that involves no external reagents. Autocatenation maintains crystallinity and can be triggered either thermally or by shear forces. The ligand used to construct these MOFs is chiral, and both racemic and enantiopure partially interpenetrated frameworks can be accessed. X-ray diffraction, nonlinear optical microscopy and theoretical calculations offer insights into the structures and dynamic behaviour of these materials and the growth mechanisms of interpenetrated MOFs.

The interpenetration of multiple sub-lattices in metal–organic frameworks (MOFs)[1,2] is a common occurrence when permitted by the lattice size and topology[3–8]. Interpenetration influences the size and shape of MOF pores, which in turn modulates their molecular sieving and storage properties[9–17]. Methods to control framework entanglement have been pursued keenly, and strategies such as using sterically encumbered ligands[18–20], low temperatures and concentrations during the framework synthesis[21], and bulky solvents[22,23] have emerged. Typically, the degree of interpenetration adopts an integral value, for example two (in a doubly interpenetrated framework) or three (in a triply interpenetrated framework). The degree of interpenetration is usually fixed when the framework is assembled; however, in rare cases it has been shown that, after synthesis, it can be modified by desolvation[24–28] or high-pressure intrusion of a liquid[29]. Here we present a family of MOFs that exhibits uncommon interpenetration behaviour. First, these frameworks sustain partial degrees of interpenetration whereby the sites of one of the two sub-lattices have fractional occupancy. The extent of their occupation, and thus the degree of partial interpenetration, can be controlled during synthesis by the reaction time and by solvent composition. Second, the non-interpenetrated materials can be transformed into their doubly interpenetrated counterparts via progressively higher partial degrees of interpenetration. This 'autocatenation' process involves no external reagents and preserves crystallinity. Partial interpenetration in these MOFs can be assessed and understood by X-ray diffraction, linear and nonlinear optical microscopy, and quantum chemistry calculations.

Results and discussion

Synthesis of MUF-9 with controlled degrees of partial interpenetration. Ligand H$_2$1 is a variant of biphenyl-4,4′-dicarboxylic acid (H$_2$bpdc) with a phenyl-substituted diazocine bridge (Fig. 1), which, to our knowledge, has not been used previously to construct MOFs. Owing to twisting along its long axis, H$_2$1 has an axial chirality. Combining *rac*-H$_2$1 with Zn(NO$_3$)$_2$ in a solvothermal reaction in *N,N*-dimethylformamide (DMF) produced [Zn$_4$O(*rac*-**1**)$_3$] (β-MUF-9 (MUF, Massey University Framework)). β-MUF-9 belongs to a cubic crystal system (space group = $Pn\bar{3}m$) and features Zn$_4$O secondary building units linked by the linear ligands into a primitive cubic (**pcu**) topology (Fig. 1 and Supplementary Fig. 34), as anticipated on the basis of related MOFs[30]. Each ligand site is occupied randomly by one of the enantiomers of ligand **1** (Supplementary Fig. 37). β-MUF-9 is doubly interpenetrated, which is unexpected given that bulky ligand substituents typically lead to non-interpenetrated frameworks[18,19,31]. The two sub-lattices are related by crystallographic symmetry, and the O atom of the Zn$_4$O cluster of each sub-lattice resides at the midpoint of the cube defined by its partner.

To explore the relationship between the composition of the reaction solvent and interpenetration in MUF-9 we carried out the reaction of H$_2$1 and Zn(NO$_3$)$_2$ in other amide solvents (Table 1 and Supplementary Table 1). Using *N,N*-dibutylformamide (DBF) produced α-MUF-9, the non-interpenetrated variant of MUF-9. This framework has close structural parallels to the individual sub-lattices of β-MUF-9. Again, each ligand site is occupied randomly by one of the two enantiomers of **1** (Supplementary Fig. 37). Reactions in *N,N*-diethylformamide (DEF) over 16 hours led to interpenetrated β-MUF-9, whereas those in *N,N*-isopropylformamide (DIF) and *N*-formylpiperidine (NFPip) generated a third phase, γ-MUF-9. Although γ-MUF-9 features the six-connected Zn$_4$O clusters observed in the α and β phases, the clusters distort slightly to produce a β-Sn (**bsn**) topology[32] (Supplementary Fig. 39). It is non-interpenetrated and racemic, with certain sites occupied specifically by one of the enantiomers and others occupied randomly by either enantiomer.

When small quantities of DMF were introduced into DBF we observed an intriguing outcome. Single-crystal X-ray diffraction (SCXRD) on the well-faceted blocks of MUF-9 that deposit during solvothermal synthesis indicates that the original space group is

[1]MacDiarmid Institute for Advanced Materials and Nanotechnology, Institute of Fundamental Sciences, Massey University, Palmerston North, New Zealand. [2]PSL Research University, Chimie ParisTech – CNRS, Institut de Recherche de Chimie Paris, Paris 75005, France. [3]Molecular Visualisation and Photonics, University of Leuven, Celestijnenlaan 200D, Heverlee, Belgium. [4]Catalysis Engineering, Department of Chemical Engineering, Delft University of Technology, Julianalaan 136, Delft 2628 BL, The Netherlands. *e-mail: s.telfer@massey.ac.nz
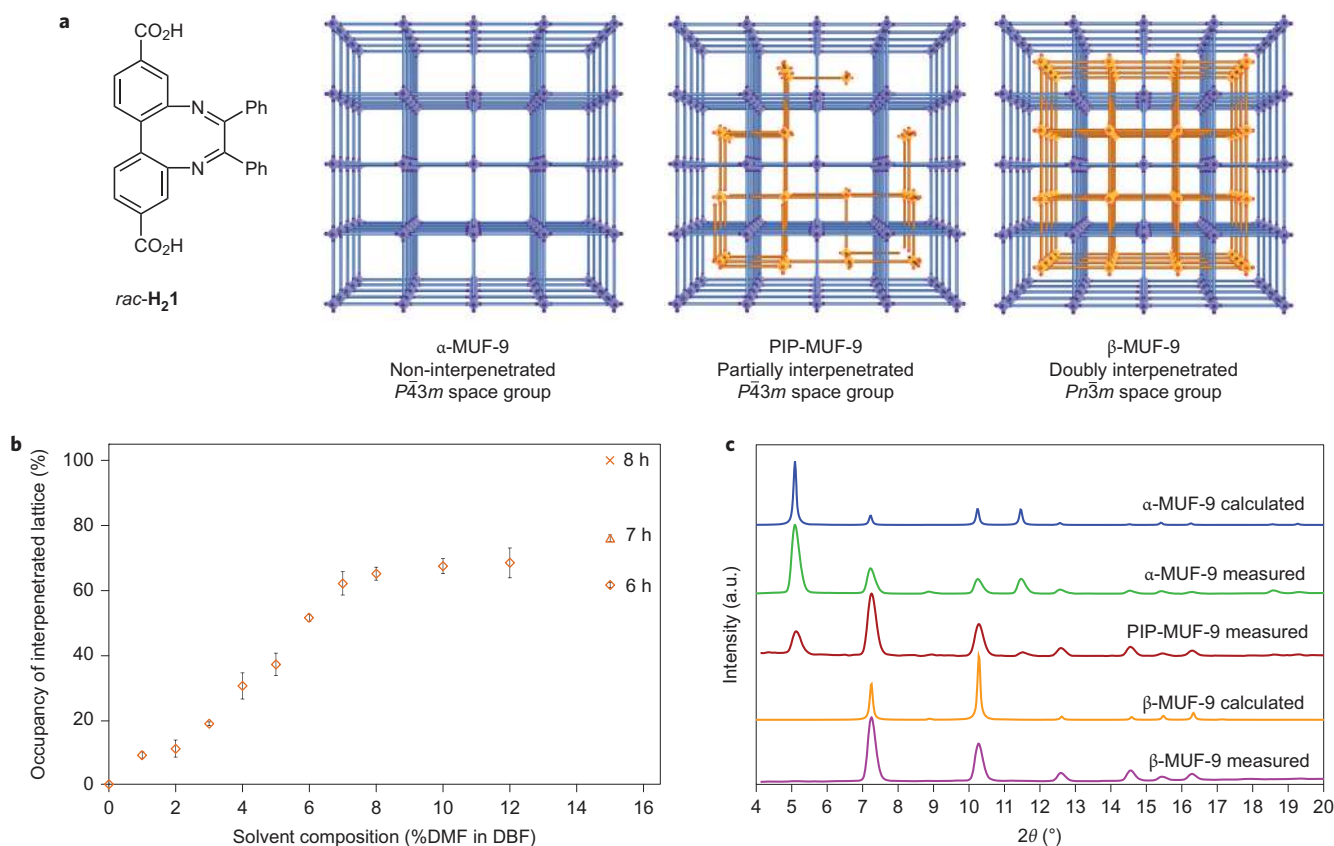
Figure 1 | MOFs with controlled degrees of interpenetration derived from the ligand _rac_-1. a, Left, structure of the ligand _rac_-**H₂1**. Right, the nature of the solvent and the reaction time determine whether the combination of _rac_-**H₂1** with Zn(NO₃)₂ produces α-MUF-9 (non-interpenetrated), PIP-MUF-9 (partially interpenetrated) or β-MUF-9 (doubly interpenetrated). The structures of α-MUF-9, PIP-MUF-9 and β-MUF-9 were determined by SCXRD. The interpenetrating sub-lattice is shown in orange. In all the frameworks the ligand sites are randomly occupied by one of the enantiomers of **1**. **b**, The composition of the reaction solvent controls the degree of partial interpenetration in MUF-9. SCXRD determined 12 different levels of partial interpenetration, given by the occupancy of the second sub-lattice The orange diamonds represent the average level of interpenetration measured by independent SCXRD measurements on three crystals from the same batch after a reaction time of six hours, and the error bars indicate the s.d. The orange triangle and orange cross show the interpenetration level after reaction times of seven and eight hours, respectively, with a 15% volume fraction of DMF. **c**, PXRD patterns (Cu Kα radiation) of α-MUF-9 (experimentally measured and calculated from the SCXRD structure), a selected example of PIP-MUF-9 and β-MUF-9 (experimentally measured and calculated from the SCXRD structure).

maintained and that the framework is partially interpenetrated: the atomic sites of the first sub-lattice are fully occupied, whereas those of the second are fractionally occupied. The occupancy of the latter sites, as deduced from crystallographic data, corresponds to the percentage of unit cells, averaged over an entire crystal, that are doubly interpenetrated. This degree of partial interpenetration is designated as PIP-##-MUF-9 where ## is a percentage.

Figure 1b illustrates how the degree of partial interpenetration is controlled by the amount of DMF in the reaction medium after a reaction time of six hours. Crystallographic datasets collected on more than 30 individual crystals (Supplementary Table 3) portray a strong dependence of the interpenetration level on the amount of DMF in the solvent mixture (Fig. 1b). The level of partial interpenetration in crystals from the same synthesis batch cluster within a narrow range. For example, three individual crystals grown from 5% DMF in DBF were found to have interpenetration levels between 33 and 39%. That a limit on the level of interpenetration of ~65% is reached over a period of six hours is evident. Extension of the reaction time beyond six hours increased the PIP level to 100% (β-MUF-9). In addition to SCXRD, the degree of interpenetration is reflected by the powder X-ray diffraction (PXRD) patterns of bulk samples (Fig. 1c and Supplementary Fig. 3). The (100) reflection at $2\theta = 5.2°$ ($d = 17.2$ Å) is intense for α-MUF-9, but systematically absent for β-MUF-9.

For PIP-MUF-9, the degree of interpenetration correlates with a progressive decrease in the intensity of the (100) reflection relative to the (110) reflection at $2\theta = 7.3°$.

Partial interpenetration can be viewed as an unusual case of structural disorder[33]. A seminal publication in 2012 described

Table 1 | Influence of the conditions on the outcome of the reaction of H₂1 with Zn(NO₃)₂.

rac-**H₂1**			Enantiopure **H₂1**		
Solvent	Time (h)	Product	Solvent	Time (h)	Product
DBF	6	α-MUF-9	DBF	16	α-MUF-10
	134	PIP-78-MUF-9		70	α-MUF-10*
DBF/DMF	6	PIP-MUF-9†	DBF/DMF	16	PIP-MUF-10†
DEF	2	PIP-71-MUF-9	DEF	16	γ-MUF-10
	16	β-MUF-9			
DMF	8	PIP-52-MUF-9	DMF	60	β-MUF-10
	16	β-MUF-9			
DIF	16	γ-MUF-9	DIF	16	γ-MUF-10
NFPip	16	γ-MUF-9	NFPip	16	γ-MUF-10
NFPyr	80	No MOF	NFPyr	120	γ-MUF-10

*An additional, unknown phase also forms. †The level of partial interpenetration is controlled by the volume fraction of DMF and the reaction time.
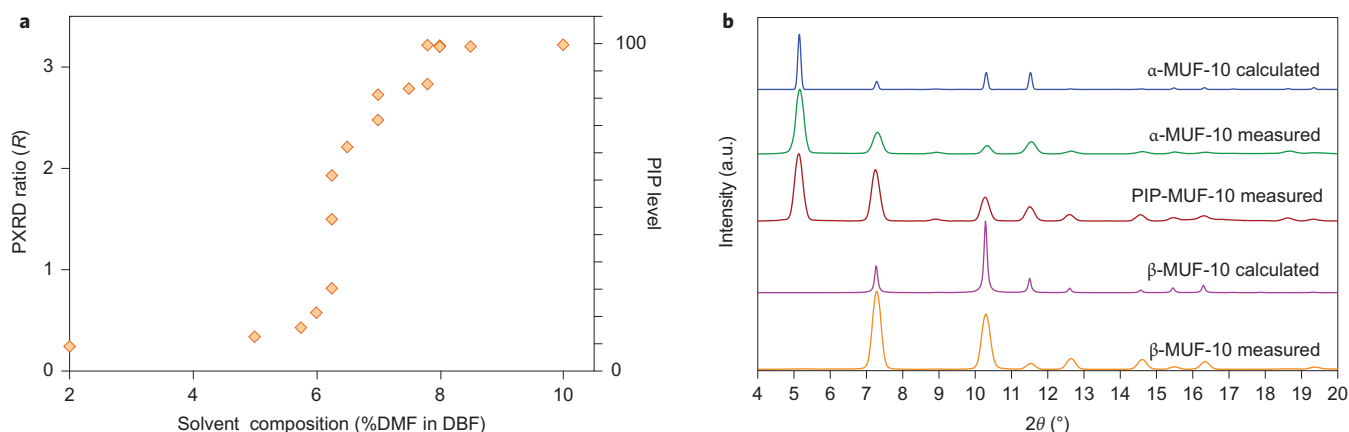
Figure 2 | MOFs with controlled degrees of interpenetration derived from ligand R-1 or S-1. a, The solvent composition determines whether the combination of enantiopure R- or S-$H_2$1 with Zn(NO$_3$)$_2$ produces α-MUF-10 (non-interpenetrated), PIP-MUF-10 (partially interpenetrated) or β-MUF-10 (doubly interpenetrated). The structures of α-MUF-10 and β-MUF-10 were determined by SCXRD, whereas the trend in the levels of interpenetration of PIP-MUF-10 can be correlated with the PXRD patterns using the ratio $R = (I^\alpha_{5.2}/I^\alpha_{7.3}) - (I^{obs}_{5.2}/I^{obs}_{7.3})$ where $I^\alpha_{5.2}$ and $I^\alpha_{7.3}$ are the intensities of the peaks of α-MUF-10 at 5.2° and 7.3°, respectively, and $I^{obs}_{5.2}$ and $I^{obs}_{7.3}$ are the observed intensities at 5.2° and 7.3°, respectively, for each PIP-MUF-10 sample. **b**, PXRD patterns (Cu Kα radiation) of α-MUF-10 (experimentally measured and calculated from the SCXRD structure), an example PIP-MUF-10 and β-MUF-10 (experimentally measured and calculated from the SCXRD structure).

NOTT-202, an indium–carboxylate MOF. The second lattice of this material has an occupancy of 75%[34]. However, the non-interpenetrated variant of NOTT-202 was not observed, and only one level of partial interpenetration was achieved. In contrast, MUF-9 provides straightforward and controlled access to materials with virtually any degree of interpenetration between zero and one.

MUF-10 is the enantiopure analogue of MUF-9 and can be synthesized using resolved R-$H_2$1 or S-$H_2$1 (Fig. 2, Table 1 and Supplementary Table 2). A high energy barrier[35] prevents racemization of the ligand during MOF synthesis. Using DMF as the reaction solvent produced the doubly interpenetrated framework β-MUF-10, whereas DBF led to the non-interpenetrated phase α-MUF-10. α-MUF-10 defines a regular **pcu** lattice, two perfectly offset copies of which are present in β-MUF-10. Switching to DEF as the solvent generated γ-MUF-10, a non-interpenetrated framework with a **bsn** topology. Several other formamide solvents—DIF, NFPip, NFPyr (N-formylpyrrolidine)—were also found to produce γ-MUF-10 (Supplementary Fig. 13). All ligand sites in the MUF-10 series are occupied by linkers with the same handedness (Supplementary Fig. 38) and, as mandated by their homochirality, all frameworks belong to chiral space groups (Supplementary Table 4).

R-$H_2$1   S-$H_2$1
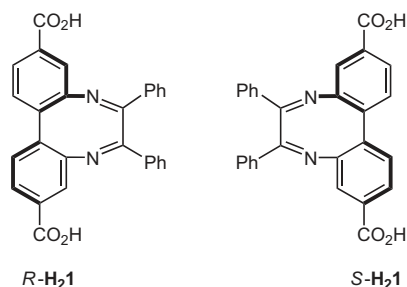
In parallel with our observation on MUF-9, partial degrees of interpenetration can be generated in MUF-10 by using small amounts of DMF in DBF as the reaction medium (Fig. 2a). The crystal quality of partially interpenetrated MUF-10 did not permit SCXRD to be used to determine the fractional occupancy of the second lattice. However, in a similar fashion to MUF-9, the (100) reflection is extinguished by the presence of the second lattice and

therefore it diminishes markedly in intensity with increasing degrees of partial interpenetration (Fig. 2b and Supplementary Fig. 10).

We also examined the effect of reaction time on the level of interpenetration in MUF-9 and MUF-10 (Table 1 and Supplementary Tables 1 and 3). For MUF-9, X-ray diffraction revealed that crystals formed at the onset of crystallization in DMF (after eight hours) and DEF (after two hours) were partially interpenetrated (52% for DMF and 71% for DEF (Table 1, Supplementary Fig. 5 and Supplementary Table 3)). Prolonging the reaction time led to an increase in the occupancy of the second sub-lattice, eventually delivering β-MUF-9 as the sole product in both solvents. In DBF, SCXRD snapshots showed that framework growth proceeds in a related way: the initially formed α-MUF-9 crystals were progressively converted into PIP-MUF-9 over a period of several days, although the PIP level plateaued at ~78% (Supplementary Table 3).

In contrast to MUF-9, α-MUF-10 completely resisted interpenetration when grown in DBF even after prolonged reaction times. Instead, a new (unknown) phase appeared in the reaction mixture after two days (Supplementary Fig. 12). In DMF/DBF mixtures, the PIP-MUF-10 crystals that formed in the early stages of the reaction gradually converted into β-MUF-10 (Supplementary Fig. 11). Thus, as for MUF-9, premeditated PIP levels in MUF-10 can be achieved simply by selecting the appropriate solvent composition and reaction time.

To examine the impact of modifications to the ligand structure on the propensity for partial interpenetration we synthesized MUF-11, MUF-12 and MUF-14 (Fig. 3). $H_2$2 and $H_2$3 behave in a similar way to $H_2$1: heating with Zn(NO$_3$)$_2$ in DBF produced MUF-11 and

MUF-11, [Zn$_4$O(**2**)$_3$]
MUF-12, [Zn$_4$O(**3**)$_3$]
MUF-14, [Zn$_4$O(**4**)$_3$]

H_2**2**, R = 4-methylphenyl
H_2**3**, R = 4-bromophenyl
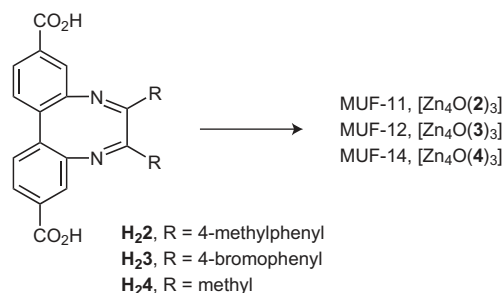H_2**4**, R = methyl

Figure 3 | Ligand functionalization. The materials MUF-11, MUF-12 and MUF-14 were synthesized from ligands H_2**2**, H_2**3** and H_2**4**, respectively.

MUF-12, respectively, which are non-interpenetrated when initially formed (about three hours), but their degree of interpenetration progressively rises over time (Supplementary Figs 14 and 15). Both β-MUF-11 and β-MUF-12 can be obtained directly by synthesis in DMF, and analysis by SCXRD revealed very close structural similarities to MUF-9. Monitoring the formation of MUF-14 in DEF demonstrated that in the early stages of the reaction α-MUF-14 was produced. Over time, PIP-MUF-14 appeared and the level of partial interpenetration increased as a function of the reaction time (Supplementary Fig. 16). Together, these experiments establish $[Zn_4OL_3]$ MOFs derived from diazocine-bridged biphenyldicarboxylate ligands as a platform of materials with diverse chemical characteristics in addition to tunable levels of partial interpenetration.

MOFs with controlled degrees of interpenetration have the potential to be useful in applications in which materials that allow both rapid mass transport and a high surface area can avoid the trade-off that typically exists between capacity and selectivity. Akin to hierarchical zeolites[36,37], the small pockets defined by the regions of interpenetration provide scope for discriminating molecular guests, whereas the large non-interpenetrated void spaces enable rapid guest diffusion. In addition, adsorption sites of high polarity (because of dangling bonds) and complex geometries will be created at the propagation fronts of the interpenetrating lattice. Among other applications, the homochirality of MUF-10 provides a means of discriminating the enantiomers of chiral guest molecules, such as pharmaceuticals and natural products[38]. Although a comprehensive examination of guest uptake by MUFs-9–14 is still in progress, TGA and ^{1}H NMR spectroscopy on MUF-9 and MUF-10 (Supplementary Figs 47–56) indicate that the non-interpenetrated frameworks incorporate more solvent than their doubly interpenetrated counterparts, as expected on the basis of their larger void volumes. The degree of interpenetration also dictates their ability to adsorb acridine orange from solution. Deep coloration of α-MUF-9 and α-MUF-10 crystals indicates a high loading of the dye (Supplementary Figs 40 and 45). As the degree of interpenetration in MUF-9 increases its capacity for acridine orange, the uptake is reduced (Supplementary Figs 41 and 42), and it is excluded from the smaller pores of β-MUF-9 and β-MUF-10 (Supplementary Figs 43 and 45).

Autocatenation of α-MUF-9 and α-MUF-10. In a process that we term autocatenation, α-MUF-9 can be transformed into its doubly interpenetrated analogue via progressively higher degrees of partial interpenetration in a single-crystal-to-single-crystal[39] phase transition (Fig. 4). No external reagents are involved and the process is irreversible. Autocatenation of α-MUF-9 can be triggered in at least three ways: (1) by heating, (2) by desolvation and (3) by mechanical shearing. In the thermal process, crystals of α-MUF-9 heated to 85 °C in DMF for 48 hours maintain their external appearance but shrink in size. The crystal volume reduces by ~50% (Fig. 4b and Supplementary Fig. 20), consistent with the expected twofold increase in density. A well-resolved set of X-ray diffraction spots, which correlates with the 17.2 Å cubic unit cell of MUF-9, is maintained by the crystals. The intensity of diffraction at high 2θ angles indicates that the structural regularity of the lattice improves as the degree of interpenetration increases (Fig. 4c). During this transformation the degree of interpenetration can be assessed by SCXRD (Fig. 4d and Supplementary Table 3).

Heating crystals of α-MUF-10 over a period of several days at 85 °C in DMF also induces autocatenation, finally producing β-MUF-10 (Supplementary Figs 26–31). A general trend in the rate of autocatenation emerges for both MUF-9 and MUF-10. An initial period in which the degree of interpenetration rises slowly is followed by a more rapid change to deliver the fully interpenetrated framework (Fig. 4d and Supplementary Fig. 27). Small quantities of water, $Zn(NO_3)_2$ or **H$_2$1** added to the DMF solution accelerate the

autocatenation of α-MUF-10 (Supplementary Fig. 27). Further observations include: (1) distinct differences in autocatenation rates exist among individual α-MUF-9 crystals heated in DMF for the same period of time (Fig. 4d); (2) directly synthesized PIP-MUF-9 converts into β-MUF-9 by autocatenation (Supplementary Fig. 17); (3) thermal autocatenation of α-MUF-9 and PIP-MUF-9 occurs in DEF, but not in DBF or in DBF/DMF 80/20 (Supplementary Figs 18, 19 and 22); (4) a dissolution–reprecipitation mechanism for the phase transition was ruled out by monitoring the interpenetration changes of a solitary crystal in a large volume of DMF in which the effects of dilution would preclude regrowth of the MOF and, furthermore, no free ligand was detectable in the supernatant during autocatenation (Supplementary Fig. 21) and (5) the propensity of α-MUF-9 to autocatenate is not shared by γ-MUF-9 (Supplementary Fig. 25).

Autocatenation of α-MUF-9 is also induced by the escape of occluded DMF from its pores. We monitored this transformation by SCXRD, which showed PIP-77-MUF-9 to be present after 100 minutes of drying and then β-MUF-9 after a further 100 minutes (Supplementary Table 3). Optical microscopy of the autocatenated crystals showed that they are cloudy pseudomorphs of the originals and reduced in volume by around 25% (Supplementary Fig. 23). This volume decrease is lower than the 50% expected, possibly owing to the formation of mesoscale voids that cause the loss of transparency. Autocatenation of α-MUF-10 is also induced by the loss of occluded DMF. Evidence for this phase change comes from changes in the PXRD patterns (Supplementary Fig. 32), and a reduction in the crystal volume of ~45% (Supplementary Fig. 33), which is close to the expected value of 50%. In the case of MUF-10 the crystals maintain both their external form and optical transparency.

Mechanochemical forces also induce autocatenation. For example, grinding crystals of α-MUF-9 suspended in DMF, using either a conventional mortar and pestle or a magnetic stir-bar, produced β-MUF-9 via progressively higher degrees of partial interpenetration (Fig. 4e and Supplementary Fig. 24). Conversely, isotropic compression at pressures of up to 0.5 GPa left α-MUF-9 unchanged.

Related examples of a post-synthetic change in interpenetration state have been reported for MOF-123[27], $[Zn_2(ndc)_2(bpy)]$[26] and $[Cd(bdc)(bpy)]$[25] (ndc, 2,6-naphthalenedicarboxylate; bpy, 4,4′-bipyridine; bdc, 1,4-benzenedicarboxylate). In the case of MOF-123, autocatenation is triggered by heating the framework to expel coordinated DMF molecules. The process is reversed on exposure to DMF. In $[Zn_2(ndc)_2(bpy)]$, a doubly interpenetrated framework converts into its triply interpenetrated analogue by desolvation as $[Cd(bdc)(bpy)]$ and switches from being non-interpenetrated to doubly interpenetrated. It has also been established that coordination bonds can be cleaved *en masse* to alter the dimensionality of coordination polymers[39,40], which is often correlated with solvent loss[41]. MUF-9 and MUF-10 go beyond these materials by showing that this transformation can be effected in an archetypal Zn_4O–carboxylate MOF and triggered by a range of stimuli. Intermediate frameworks with partial degrees of interpenetration can be isolated and characterized along the autocatenation pathway.

Nonlinear optical microscopy. Second harmonic generation (SHG) microscopy serves as a sensitive probe of local framework organization because its efficiency depends strongly on point group symmetry[42,43]. SHG is forbidden in centrosymmetric materials, and therefore it provides a high contrast between non-centrosymmetric α-MUF-9 (Fig. 5a) and centrosymmetric β-MUF-9 (Fig. 5d) crystals. Variation in the SHG intensity for different crystals within the same image is expected because the intensity of the signal depends on the orientation of the crystal with respect to the plane of polarization of the incident laser light. As portions of the PIP-MUF-9 crystals are centrosymmetric, weaker SHG responses compared with those of α-MUF-9 are
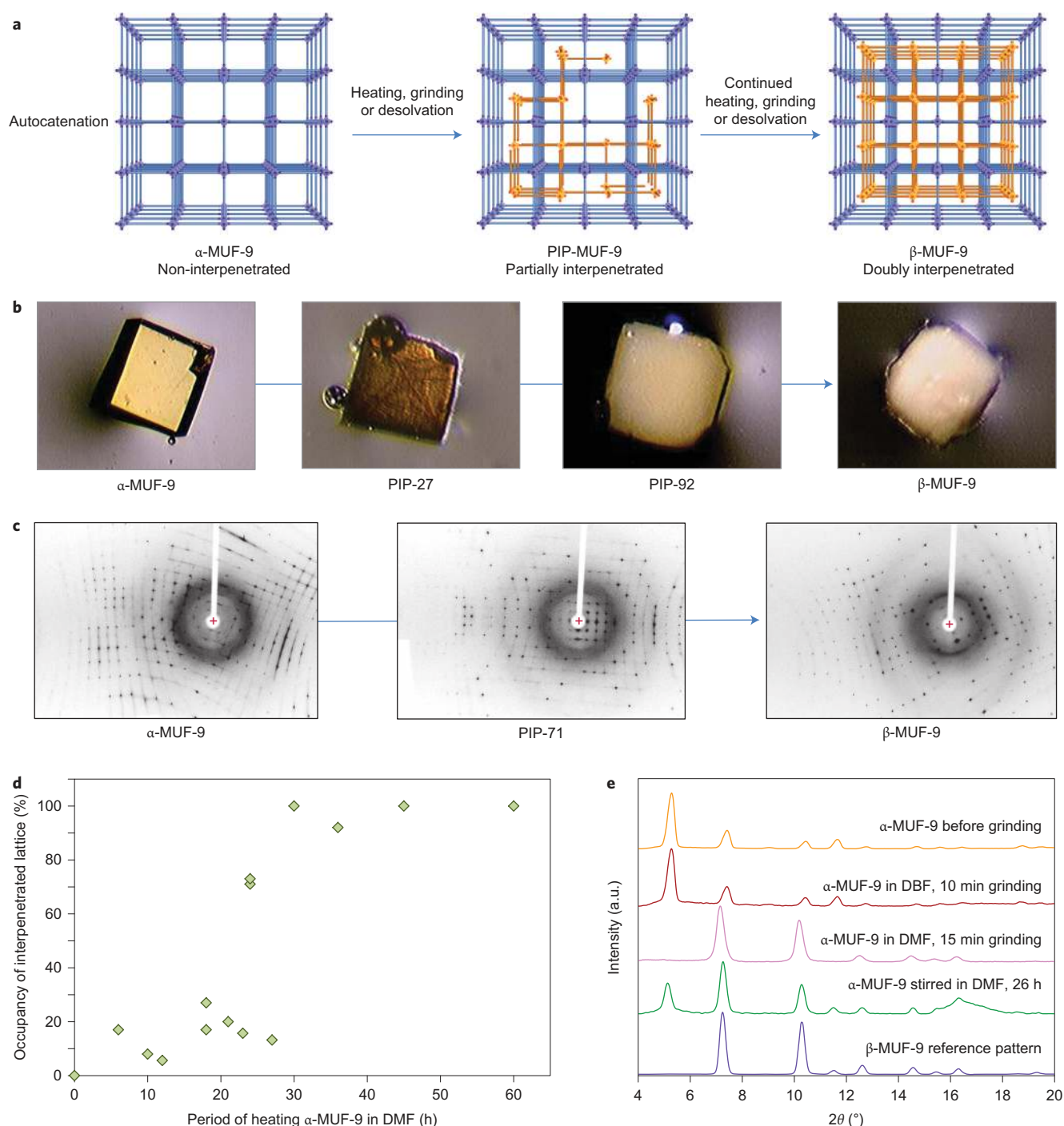
Figure 4 | Autocatenation in MUF-9. a, α-MUF-9 converts into β-MUF-9 via PIP-MUF-9 by a single-crystal-to-single-crystal autocatenation process. Crystals with progressively higher degrees of partial interpenetration are produced by heating, grinding or desolvation. **b**, Optical micrographs of a crystal undergoing this conversion by heating to 85 °C in DMF. **c**, X-ray diffraction images demonstrate that thermally induced autocatenation is a single-crystal-to-single-crystal process. **d**, For thermal autocatenation, the level of interpenetration, as determined by the occupancy of the interpenetrating lattice determined by SCXRD, is controlled by the heating time. A degree of variability is observed between individual crystals heated for the same length of time. **e**, PXRD patterns (Cu Kα radiation) of α-MUF-9 after grinding in a mortar and pestle in DBF, which produced no structural change (red trace), after grinding in DMF, which resulted in conversion to β-MUF-9 (pink trace) and after mechanical grinding using a magnetic stir-bar, which produced PIP-MUF-9 (green trace).

observed (Fig. 5b,c). Two-photon fluorescence (2PF) microscopy images materials regardless of their point group symmetry. 2PF signals are generated by all frameworks, although they become significantly weaker as the level of interpenetration rises.

Although X-ray crystallography gives a reliable estimate of the overall level of interpenetration in PIP-MUF-9 crystals, it provides an averaged picture and cannot spatially resolve the interpenetrated regions. In contrast, SHG microscopy is an ideal tool for determining whether the interpenetrating sub-lattice is present uniformly throughout MUF-9 crystals or is confined to certain zones. The synthesis of MUF-9 in DBF was monitored by SHG microscopy over a period of days as the interpenetrating lattice grew in (Supplementary Fig. 58). For PIP-15-MUF-9, the SHG response was initially observed to be uniform, which implies that growth
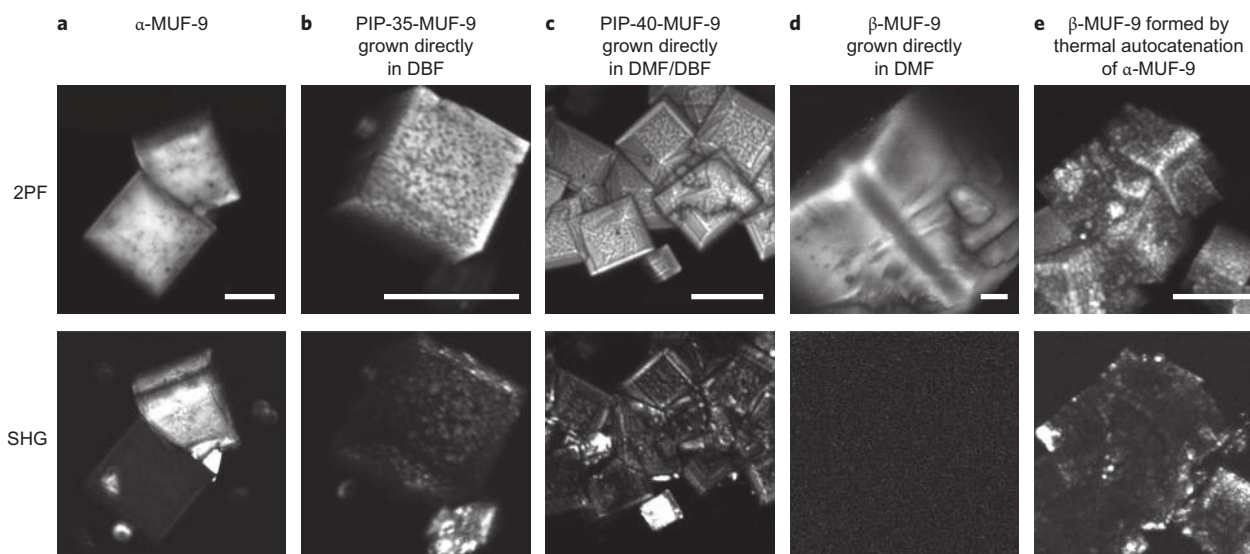
Figure 5 | Characteristics of frameworks with various levels of interpenetration produced by different methods. a–e, SHG and 2PF micrographs of α-MUF-9 crystals (**a**), partially interpenetrated MUF-9 crystals grown in DBF (**b**) or DMF/DBF (**c**), β-MUF-9 grown directly in DMF (**d**) and β-MUF-9 formed by the thermal autocatenation of α-MUF-9 (**e**). The SHG response of the crystals decreases with increasing levels of interpenetration, which is consistent with the difference in symmetry between α-MUF-9 (non-centrosymmetric) and β-MUF-9 (centrosymmetric). Scale bars, 30 μm.

of the second framework was not localized spatially. Over time, the level of partial interpenetration increased and the 2PF and SHG responses became patchier and domains several microns in size appeared (for example, PIP-35-MUF-9 in Fig. 5b). We ascribe this inhomogeneity to crystal zones with differing degrees of interpenetration. As expected, for the more highly interpenetrated crystals an increased spatial uniformity of the SHG signal is coupled to its overall attenuation (Supplementary Fig. 58). The 2PF and SHG responses from PIP-40-MUF-9 crystals grown directly in DMF/DBF were patchy across individual crystals, which reveals the existence of zones a few microns in size with differing degrees of interpenetration (Fig. 5c). As anticipated, the SHG signal intensity from α-MUF-9 crystals decreased steadily on autocatenation (Fig. 5e and Supplementary Figs 59 and 60). This signal reduction occurred uniformly throughout the crystals, which implies that the spatial distribution of interpenetrated crystal regions is homogeneous.

Theoretical characterization. To better understand the interpenetration behaviour of MUF-9 and MUF-10, we performed quantum chemical calculations at the density functional theory level on two guest-free models of MUF-10. For the purpose of comparison, we also performed calculations on γ-MUF-10, as well as two archetypal MOFs with the **pcu** topology, IRMOF-9 (doubly interpenetrated [$Zn_4O(bpdc)_3$]) and IRMOF-10 (non-interpenetrated [$Zn_4O(bpdc)_3$]). All the structures were energy-minimized fully; the resulting coordinates are given in the Supplementary Information and their crystallographic parameters summarized in Supplementary Table 5.

The calculations confirm that evacuated α-MUF-10 is a meta-stable phase with respect to β-MUF-10, with an 'interpenetration enthalpy' of 259 kJ mol^{-1} per Zn_4O unit. This is much larger than the corresponding enthalpy difference between IRMOF-10 and IRMOF-9, which we calculated to be 77 kJ mol^{-1}. This difference can be ascribed to the non-covalent interligand contacts between the pendant phenyl rings of ligands from different sub-lattices in MUF-10 (Supplementary Fig. 35). We also calculated the structure and relative energy of γ-MUF-10: it falls slightly (9.1 kJ mol^{-1}) below that of the α-MUF-10 phase, being intermediate between α-MUF-10 and β-MUF-10.

Calculations of the second-order elastic tensors can shed light on the mechanical properties of MOF lattices[44], in particular their mechanical stability and their propensity for structural transitions on compression, shear forces[45] or guest evacuation[46]. This tensorial analysis, although performed on the MIL-53 and some other flexible MOFs[44,47], is used here for the first time in evaluating the impact of interpenetration. The full tensors of α- and β-MUF-10 are given in Supplementary Tables 6 and 7, and their calculated mechanical properties are summarized in Supplementary Table 8. As calculated for related porous MOFs[48], α-MUF-10 is extremely soft, with an average Young's modulus of 3.7 GPa and a shear modulus of 1.3 GPa. In addition, it shows a highly anisotropic elastic behaviour characteristic of flexible MOFs, so-called soft porous crystals, that undergo stimuli-induced structural transitions[49–52]. The softest mode of the structure corresponds to an extremely low modulus of 0.13 GPa for the rhombohedral shear of the α-MUF-10 structure (Supplementary Movie 1). The calculated average bulk modulus is 6.8 GPa, significantly higher than the low shear modulus, which is in accord with experiments showing that the non-interpenetrated structures are unchanged by isotropic compression at moderate pressures.

In comparison with α-MUF-10, the calculated elastic properties of interpenetrated β-MUF-10 depict a much stiffer material, with a bulk modulus of 11.7 GPa, average Young's modulus of 8.9 GPa and shear modulus of 3.2 GPa. This is consistent with the generally observed correlation between elastic properties and framework density, often seen as a function of guest loading and pore topology[45,53], and as previously calculated in the specific case of MOF-14 (ref. 54). In addition to being stiffer than the non-interpenetrated phase, β-MUF-10 also shows a much lower anisotropy of its elastic properties, as is typical for inflexible MOFs. Its softest deformation mode is also a shearing mode, but its elastic modulus of 1.0 GPa indicates a mechanical stability that is an order of magnitude higher than that of α-MUF-10.

Partial interpenetration, framework growth and autocatenation behaviour. Interpenetration in MOFs is a well-studied phenomenon, but partial interpenetration has only been reported on one previous occasion[34]. Why is partial interpenetration such a rare occurrence, as previously it has not been observed in the very well-studied[18,19,23,55] family of [$Zn_4O(bpdc)_3$] derivatives, yet is

readily manifest in the MOFs reported herein? Drawing on both our experimental and computational results, we propose the following two-part explanation. (1) As partially interpenetrated lattices necessarily have dangling bonds in the form of open (or solvent-filled) coordination sites on their Zn_4O clusters and non-coordinated carboxylate groups, they are likely to incur a significant energy penalty. This penalty must be offset by some form of energetic stabilization. Owing to the distinctive structural characteristics of their diazocine bridge, the pendant groups of ligands **1–4** extend laterally from their long axis. This allows the sub-lattices of MUFs-9–14 to engage in non-covalent interactions (Supplementary Figs 35 and 36), which provide the energetic stabilization required to sustain partial interpenetration. (2) To observe partially interpenetrated frameworks the growth rate of the host sub-lattice must exceed that of the interpenetrating sub-lattice. The growth rates of the two sub-lattices of MUFs-9–14 are similar in DMF, and therefore when crystals reach a size amenable to SCXRD the level of interpenetration is already high. In the bulkier DBF, the first sub-lattice crystallizes within hours, whereas the propagation of the interpenetrating sub-lattice is much slower, which allows partially interpenetrated crystals to be harvested. Small quantities of DMF introduced to DBF systematically accelerate the growth of the interpenetrating sub-lattice to control the degree of partial interpenetration.

Our collective results help address questions in the field of coordination polymers and MOFs regarding the growth mechanism of interpenetrated frameworks, which is thought to occur either by (1) concurrent growth of the intepenetrating sub-lattices, or (2) sequential growth that involves the infiltration of an interpenetrating sub-lattice through the pores of an initially formed host. Our observations clearly establish that mechanism (2) is feasible. A third, hitherto unrecognized, growth mechanism has also come to light. Here, thermal autocatenation occurs simultaneously with lattice growth. This process follows Ostwald's rule of stages[56,57] in that, as a crystal grows, an initial metastable non-interpenetrated phase cascades down to the final thermodynamically preferred doubly interpenetrated product via a series of intermediate partially interpenetrated states. This reaction pathway permits interpenetrated MOFs to grow even though their direct formation may be inhibited by low reaction temperatures or low concentrations, or where the transport of fresh reagents, such as bulky ligands, through the pores of a growing crystal is restricted. Our contrasting observations on the growth of MUF-9 in various solvents are consistent with this third mechanism. Given a suitably long reaction time, β-MUF-9 is produced in DMF and DEF, but the PIP level plateaus at ~80% in DBF. In DMF and DEF, thermal autocatenation is possible, and therefore full occupancy of the interpenetrating sub-lattice can be achieved by the growth of a non-interpenetrated crystal region followed by its autocatenation. Conversely, as thermal autocatenation is not possible in DBF, the growth of the interpenetrating sub-lattice in this solvent relies solely on the diffusion of the framework components through the pores of the parent network. Propagation of this sub-lattice is self-inhibiting (on steric grounds), which explains why certain crystal regions remain non-interpenetrated.

Autocatenation of MUF-9 and MUF-10 reveals a surprising degree of pliability for Zn_4O–carboxylate MOFs. Single crystallinity is maintained during a structural reconfiguration that requires large numbers of metal–ligand bonds to be cleaved transiently. Our observations indicate that the genesis and propagation of the interpenetrating sub-lattice has parallels with the conventional model of crystal nucleation. As the degree of autocatenation is not a smooth function of heating time (Fig. 4d) it appears to be triggered in individual crystals at different times. This is consistent with nucleation of the interpenetrating sub-lattice being a stochastic process with an activation energy barrier. Nucleation is followed by sub-lattice growth. Initially, the interpenetration level rises only slowly, because this sub-lattice only has a small number of attachment points, but it accelerates over time as its growth front becomes more extensive.

The insights provided by computational chemistry allow us draw conclusions regarding the propensity for α-MUF-9 and α-MUF-10 to autocatenate by quantitatively evaluating the lowest shear modulus in both structures. These non-interpenetrated lattices are calculated to have low shear moduli, which explains why they autocatenate when subjected to the large shear forces and internal stresses that are produced by heating, grinding or evaporation of the solvent trapped in their pores. MOFs are commonly observed to be mechanically unstable towards such forces, but they tend to collapse into a dense and/or amorphous material[58,59]. In the case of MUF-9 and MUF-10, the non-interpenetrated frameworks are propelled along an autocatenation trajectory that links the metastable non-interpenetrated framework with its doubly interpenetrated counterpart. The stabilizing non-covalent interactions that develop on the interpenetration of the sub-lattices lower the energy barrier to this transformation and stabilize the interpenetrated product. We anticipate that these computational insights will assist the discovery of other frameworks that have a propensity for autocatenation.

Outlook

In summary, the degree of partial interpenetration can be controlled precisely in a family of MOFs by both direct synthesis and by autocatenation, a progressive transformation of a metastable non-interpenetrated lattice into a doubly interpenetrated framework. Partially interpenetrated MOFs are stabilized by non-covalent interactions between the sub-lattices, and can be isolated when the solvent composition differentiates the growth rates of the host and interpenetrating lattices. These observations offer insight on the structure, reactivity and growth mechanisms of MOFs. We envisage that the combination of high selectivity in the interpenetrated regions and rapid diffusion in the non-interpenetrated regions may in future developments be used to optimize the uptake and discrimination of molecular guests, including chiral molecules, by this platform of materials.

Methods

Experimental methods, computational and crystallographic data, and additional details are freely available in the Supplementary Information.

References

1. Furukawa, H., Cordova, K. E., O'Keeffe, M. & Yaghi, O. M. The chemistry and applications of metal–organic frameworks. *Science* **341,** 6149 (2013).
2. Allendorf, M. D. & Stavila, V. Crystal engineering, structure–function relationships, and the future of metal–organic frameworks. *CrystEngComm* **17,** 229–246 (2015).
3. Batten, S. R. Topology of interpenetration. *CrystEngComm* **3,** 67–72 (2001).
4. Batten, S. R. & Robson, R. Interpenetrating nets: ordered, periodic entanglement. *Angew. Chem. Int. Ed.* **37,** 1460–1494 (1998).
5. Zhang, S.-Y., Zhang, Z. & Zaworotko, M. J. Topology, chirality and interpenetration in coordination polymers. *Chem. Commun.* **49,** 9700–9703 (2013).
6. Jiang, H.-L., Makal, T. A. & Zhou, H.-C. Interpenetration control in metal–organic frameworks for functional applications. *Coord. Chem. Rev.* **257,** 2232–2249 (2013).
7. Blatov, V. A., Carlucci, L., Ciani, G. & Proserpio, D. M. Interpenetrating metal–organic and inorganic 3D networks: a computer-aided systematic investigation. Part I. Analysis of the Cambridge Structural Database. *CrystEngComm* **6,** 378–395 (2004).
8. Baburin, I. A. *et al.* Interpenetrating metal–organic and inorganic 3D networks: a computer-aided systematic investigation. Part II. Analysis of the Inorganic Crystal Structure Database (ICSD). *J. Solid State Chem.* **178,** 2452–2474 (2005).
9. Nugent, P. *et al.* Porous materials with optimal adsorption thermodynamics and kinetics for CO_2 separation. *Nature* **495,** 80–84 (2013).

10. Rowsell, J. L. C. & Yaghi, O. M. Effects of functionalization, catenation, and variation of the metal oxide and organic linking units on the low-pressure hydrogen adsorption properties of metal–organic frameworks. *J. Am. Chem. Soc.* **128**, 1304–1315 (2006).

11. Maji, T. K., Matsuda, R. & Kitagawa, S. A flexible interpenetrating coordination framework with a bimodal porous functionality. *Nature Mater.* **6**, 142–148 (2007).

12. Park, T.-H., Koh, K., Wong-Foy, A. G. & Matzger, A. J. Nonlinear properties in coordination copolymers derived from randomly mixed ligands. *Cryst. Growth Des.* **11**, 2059–2063 (2011).

13. Bureekaew, S. *et al.* Control of interpenetration for tuning structural flexibility influences sorption properties. *Angew. Chem. Int. Ed.* **49**, 7660–7664 (2010).

14. Feldblyum, J. I. *et al.* Interpenetration, porosity, and high-pressure gas adsorption in Zn₄O(2,6-naphthalene dicarboxylate)₃. *Langmuir* **29**, 8146–8153 (2013).

15. Ma, S. *et al.* Framework-catenation isomerism in metal–organic frameworks and its impact on hydrogen uptake. *J. Am. Chem. Soc.* **129**, 1858–1859 (2007).

16. Li, B., Wen, H.-M., Zhou, W. & Chen, B. Porous metal–organic frameworks for gas storage and separation: what, how, and why? *J. Phys. Chem. Lett.* **5**, 3468–3479 (2014).

17. Liu, B. *et al.* Enhanced adsorption selectivity of hydrogen/methane mixtures in metal–organic frameworks with interpenetration: a molecular simulation study. *J. Phys. Chem. C* **112**, 9854–9860 (2008).

18. Deshpande, R. K., Waterhouse, G. I. N., Jameson, G. B. & Telfer, S. G. Photolabile protecting groups in metal–organic frameworks: preventing interpenetration and masking functional groups. *Chem. Commun.* **48**, 1574–1576 (2012).

19. Deshpande, R. K., Minnaar, J. L. & Telfer, S. G. Thermolabile groups in metal–organic frameworks: suppression of network interpenetration, post-synthetic cavity expansion and protection of reactive functional groups. *Angew. Chem. Int. Ed.* **47**, 4598–4602 (2010).

20. Henke, S. *et al.* Zinc-1,4-benzenedicarboxylate-bipyridine frameworks—linker functionalization impacts network topology during solvothermal synthesis. *J. Mater. Chem.* **22**, 909–918 (2012).

21. Zhang, J. *et al.* Temperature and concentration control over interpenetration in a metal–organic material. *J. Am. Chem. Soc.* **131**, 17040–17041 (2009).

22. Falkowski, J. M., Wang, C., Liu, S. & Lin, W. Actuation of asymmetric cyclopropanation catalysts: reversible single-crystal to single-crystal reduction of metal–organic frameworks. *Angew. Chem.* **123**, 8833–8837 (2011).

23. Rankine, D. *et al.* Control of framework interpenetration for *in situ* modified hydroxyl functionalised IRMOFs. *Chem. Commun.* **48**, 10328–10330 (2012).

24. Aggarwal, H., Das, R. K., Bhatt, P. M. & Barbour, L. J. Isolation of a structural intermediate during switching of degree of interpenetration in a metal–organic framework. *Chem. Sci.* **6**, 4986–4992 (2015).

25. Aggarwal, H., Lama, P. & Barbour, L. J. Transformation from non- to double-interpenetration in robust Cd(II) doubly-pillared-layered metal–organic frameworks. *Chem. Commun.* **50**, 14543–14546 (2014).

26. Aggarwal, H., Bhatt, P. M., Bezuidenhout, C. X. & Barbour, L. J. Direct evidence for single-crystal to single-crystal switching of degree of interpenetration in a metal–organic framework. *J. Am. Chem. Soc.* **136**, 3776–3779 (2014).

27. Choi, S. B. *et al.* Reversible interpenetration in a metal–organic framework triggered by ligand removal and addition. *Angew. Chem. Int. Ed.* **51**, 8791–8795 (2012).

28. Zhang, J.-P., Lin, Y.-Y., Zhang, W.-X. & Chen, X.-M. Temperature- or guest-induced drastic single-crystal-to-single-crystal transformations of a nanoporous coordination polymer. *J. Am. Chem. Soc.* **127**, 14162–14163 (2005).

29. Lapidus, S. H., Halder, G. J., Chupas, P. J. & Chapman, K. W. Exploiting high pressures to generate porosity, polymorphism, and lattice expansion in the nonporous molecular framework Zn(CN)₂. *J. Am. Chem. Soc.* **135**, 7621–7628 (2013).

30. Eddaoudi, M. *et al.* Systematic design of pore size and functionality in isoreticular MOFs and their application in methane storage. *Science* **295**, 469–472 (2002).

31. Lun, D. J., Waterhouse, G. I. N. & Telfer, S. G. A general thermolabile protecting group strategy for organocatalytic metal–organic frameworks. *J. Am. Chem. Soc.* **133**, 5806–5809 (2011).

32. O'Keeffe, M., Peskov, M. A., Ramsden, S. J. & Yaghi, O. M. The Reticular Chemistry Structure Resource (RCSR) database of, and symbols for, crystal nets. *Acc. Chem. Res.* **41**, 1782–1789 (2008).

33. Cairns, A. B. & Goodwin, A. L. Structural disorder in molecular framework materials. *Chem. Soc. Rev.* **42**, 4881–4893 (2013).

34. Yang, S. *et al.* A partially interpenetrated metal–organic framework for selective hysteretic sorption of carbon dioxide. *Nature Mater.* **11**, 710–716 (2012).

35. Allinger, N. L., Szkrybalo, W. & DaRooge, M. A. On the barrier to inversion of cyclooctatetraene. The thermal decomposition of dibenzo[e,g][1,4]diazocine. *J. Med. Chem.* **28**, 3007–3010 (1963).

36. Moller, K. & Bein, T. Mesoporosity—a new dimension for zeolites. *Chem. Soc. Rev.* **42**, 3689–3707 (2013).

37. Wei, Y., Parmentier, T. E., de Jong, K. P. & Zecevic, J. Tailoring and visualizing the pore architecture of hierarchical zeolites. *Chem. Soc. Rev.* **44**, 7234–7261 (2015).

38. Nguyen, L. A., He, H. & Pham-Huy, C. Chiral drugs: an overview. *Int. J. Biomed. Sci.* **2**, 85–100 (2006).

39. Zhang, J.-P. *et al.* Single-crystal X-ray diffraction studies on structural transformations of porous coordination polymers. *Chem. Soc. Rev.* **43**, 5789–5814 (2014).

40. Stylianou, K. C. *et al.* Dimensionality transformation through paddlewheel reconfiguration in a flexible and porous Zn-based metal–organic framework. *J. Am. Chem. Soc.* **134**, 20466–20478 (2012).

41. Chesman, A. S. R., Turner, D. R., Deacon, G. B. & Batten, S. R. Transformation of a 1D to 3D coordination polymer mediated by low temperature lattice solvent loss. *Chem. Commun.* **46**, 4899–4901 (2010).

42. Van der Veen, M. A., Verbiest, T. & De Vos, D. E. Probing microporous materials with second-harmonic generation. *Micropor. Mesopor. Mater.* **166**, 102–108 (2013).

43. Van der Veen, M. A., Vermoortele, F., De Vos, D. E. & Verbiest, T. Point group symmetry determination via observables revealed by polarized second-harmonic generation microscopy. *Anal. Chem.* **84**, 6378–6385 (2012).

44. Ortiz, A. U., Boutin, A., Fuchs, A. H. & Coudert, F.-X. Anisotropic elastic properties of flexible metal–organic frameworks: how soft are soft porous crystals? *Phys. Rev. Lett.* **109**, 195502 (2012).

45. Ortiz, A. U., Boutin, A., Fuchs, A. H. & Coudert, F.-X. Investigating the pressure-induced amorphization of zeolitic imidazolate framework ZIF-8: mechanical instability due to shear mode softening. *J. Phys. Chem. Lett.* **4**, 1861–1865 (2013).

46. Bouëssel du Bourg, L., Ortiz, A. U., Boutin, A. & Coudert, F.-X. Thermal and mechanical stability of zeolitic imidizolate frameworks polymorphs. *APL Mater.* **2**, 124110 (2014).

47. Ortiz, A. U., Boutin, A., Fuchs, A. H. & Coudert, F.-X. Metal–organic frameworks with wine-rack motif: what determines their flexibility and elastic properties? *J. Chem. Phys.* **138**, 174703 (2013).

48. Kuc, A., Enyashin, A. & Seifert, G. Metal–organic frameworks: structural, energetic, electronic, and mechanical properties. *J. Phys. Chem. B* **111**, 8179–8186 (2007).

49. Coudert, F.-X. Responsive metal–organic frameworks and framework materials: under pressure, taking the heat, in the spotlight, with friends. *Chem. Mater.* **27**, 1905–1916 (2015).

50. Horike, S., Shimomura, S. & Kitagawa, S. Soft porous crystals. *Nature Chem.* **1**, 695–704 (2010).

51. Schneemann, A. *et al.* Flexible metal–organic frameworks. *Chem. Soc. Rev.* **43**, 6062–6096 (2014).

52. Li, C.-P., Chen, J., Liu, C.-S. & Du, M. Dynamic structural transformations of coordination supramolecular systems upon exogenous stimulation. *Chem. Commun.* **51**, 2768–2781 (2015).

53. Tan, J. C. & Cheetham, A. K. Mechanical properties of hybrid inorganic–organic framework materials: establishing fundamental structure–property relationships. *Chem. Soc. Rev.* **40**, 1059–1080 (2011).

54. Klein, N. *et al.* Route to a family of robust, non-interpenetrated metal–organic frameworks with pto-like topology. *Chem. Eur. J.* **17**, 13007–13016 (2011).

55. Burrows, A. D., Frost, C., Mahon, M. F. & Richardson, C. Post-synthetic modification of tagged metal–organic frameworks. *Angew. Chem. Int. Ed.* **47**, 8482–8486 (2008).

56. Ostwald, W. Studien ber die Bildung und Umwandlung fester Körper. *Z. Phys. Chem.* **22**, 289–330 (1897).

57. Threlfall, T. Structural and thermodynamic explanations of Ostwald's rule. *Org. Process Res. Dev.* **7**, 1017–1027 (2003).

58. Farha, O. K. & Hupp, J. T. Rational design, synthesis, purification, and activation of metal–organic framework materials. *Acc. Chem. Res.* **43**, 1166–1175 (2010).

59. Bennett, T. D. & Cheetham, A. K. Amorphous metal–organic frameworks. *Acc. Chem. Res.* **47**, 1555–1562 (2014).

Acknowledgements

Author contributions

A.F., L.L., D.P., S.J.T., S.V.C., M.A.v.d.V., T.V. and S.G.T. designed the experiments, carried out the experimental work and interpreted the experimental data. F.X.C. performed the theoretical calculations and analysed the results. S.G.T. coordinated the writing of the manuscript with input from all authors.

Additional information

Supplementary information and chemical compound information are available in the online version of the paper. Reprints and permissions information is available online at www.nature.com/reprints. Correspondence and requests for materials should be addressed to S.G.T.

Competing financial interests

The authors declare no competing financial interests.